JOURNAL OF GEOPHYSICAL RESEARCH: SPACE PHYSICS, VOL. 118, 7635–7642, doi:10.1002/2013JA018876, 2013

Directionality and variability of energetic neutral hydrogen fluxes observed by Mars Express

X.-D. Wang,[1] S. Barabash,[1] Y. Futaana,[1] A. Grigoriev,[2] and P. Wurz[3]

Received 19 March 2013; revised 4 November 2013; accepted 6 November 2013; published 11 December 2013.

[1] Using data collected by the neutral particle detector of the analyzer of space plasmas and energetic atoms on board Mars Express, we establish the global morphology of hydrogen energetic neutral atom (ENA) fluxes. The observations were conducted in March–July 2004 and reveal that low flux ENAs ($< 5 \times 10^5$ cm^{-2}s^{-1}sr^{-1}) are emitted roughly isotropically from the dayside of the planet. These ENA emissions originate from the backscattering of the hydrogen ENAs produced by the charge exchange of the upstream solar wind in the extended Martian exosphere. ENAs of higher fluxes are emitted preferentially in the directions perpendicular to the undisturbed solar wind velocity. This population is due to the charge exchange of the magnetosheath plasma. At a great distance, these ENA emissions resemble a thick layer or a wall. The emissions are enhanced in the direction opposite to the convective electric field ($\mathbf{E_c}$). This enhancement reflects the asymmetric shape of the induced magnetic boundary that is close to the planet hemisphere where the $\mathbf{E_c}$ points toward the Sun-Mars line ($-\mathbf{E_c}$ hemisphere). The ENA flux shows a positive correlation with the solar wind dynamic pressure. The asymmetry in the ENA emissions is modest during quiet solar wind conditions but becomes more pronounced when the solar wind dynamic pressure increases.

Citation: Wang, X.-D., S. Barabash, Y. Futaana, A. Grigoriev, and P. Wurz (2013), Directionality and variability of energetic neutral hydrogen fluxes observed by Mars Express, *J. Geophys. Res. Space Physics*, *118*, 7635–7642, doi:10.1002/2013JA018876.

1. Introduction

[2] Energetic neutral atoms (ENAs) are generated via the charge exchange process, where energetic ions (> 10 eV) are neutralized by receiving electrons from background neutral gas. The charge-exchanged ENAs maintain the composition, momentum, and energy of their parent ions and travel along straight lines because their energy is much higher than that of the gravitational potential of the central body and the radiation pressure. This similarity to photons allows for the global imaging and remote monitoring of the ENA production region. The ENA fluxes are given by line-of-sight integrals over the plasma and neutral gas distributions. Therefore, the ENAs can serve as a diagnostic tool to study plasma and neutral gas distributions. ENA detectors have been flown on board spacecraft studying the Earth [*Pollock et al.*, 2000; *Moore et al.*, 2000; *Mitchell et al.*, 2000], the Saturnian system [*Krimigis et al.*, 2004], Mars [*Barabash et al.*, 2006], Venus [*Barabash et al.*, 2007], the Moon [*Barabash et al.*, 2009], and the heliosheath [*McComas et al.*, 2009]. The observed ENA emissions are generally presented as images showing the detected ENA flux as a function of the viewing direction from different vantage points. The ENA emissions from an elementary volume in space are usually anisotropic, in contrast to photon emissions, because the parent plasmas are anisotropic with respect to the direction of the magnetic field. Therefore, images from different vantage points are needed to extract the plasma distribution correctly.

[3] When the upstream solar wind protons flow around Mars, these protons first interact with the hydrogen exosphere, which extends well beyond the bow shock (e.g., see the review by *Futaana et al.* [2011] on ENA production on Mars). The charge exchange in this region results in the solar wind ENAs, a beam of hydrogen ENAs coaligned with the solar wind of the same energy [*Barabash et al.*, 1995; *Holmström et al.*, 2002]. The solar wind protons pass through the bow shock, become thermalized, and form a subsonic magnetosheath flow around the induced magnetosphere boundary (IMB). The magnetosheath protons that exchange charges with the even denser exosphere create ENA fluxes tangential to the streamlines, but these fluxes are strongly spread due to the high temperature [*Barabash et al.*, 1995; *Holmström et al.*, 2002]. The planetary neutrals that lose an electron in the charge-exchange reaction (or via photoionization) are picked up by the magnetic field of the solar wind and may exchange charges again with the exospheric gas, thus producing planetary ENAs [*Luhmann and Kozyra*, 1991]. ENAs propagating toward the planet may collide with exospheric particles and then scatter, thus creating an ENA albedo [*Kallio and Barabash*, 2001; *Kallio and Janhunen*, 2001]. The hypothetical dust and the neutral tori of Phobos and Deimos might also be potential sources of ENAs

---

[1] Swedish Institute of Space Physics, Kiruna, Sweden.
[2] Space Research Institute, Moscow, Russia.
[3] Physikalisches Institut, Universität Bern, Bern, Switzerland.

Corresponding author: X.-D. Wang, Swedish Institute of Space Physics, Rymdcampus 1, Kiruna, SE-981 92, Sweden. (wang@irf.se)

2169-9380/13/10.1002/2013JA018876

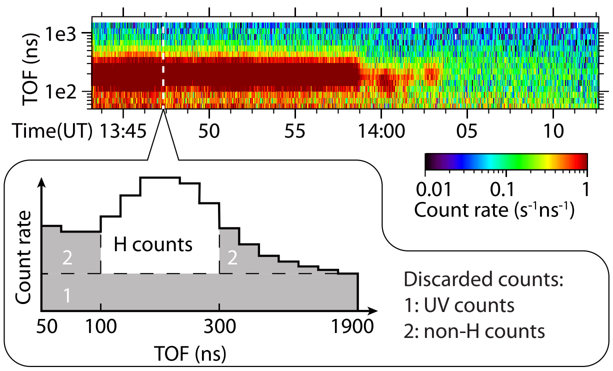

Figure 1. (top) A sample TOF-time spectrum of NPD1 Dir1. (in the bubble) A sample TOF spectrum. The gray areas represent the UV background (1) and TOF data that are filtered out for being too short or too long (2). The white areas are counts that are valid for this study.

[*Barabash et al.*, 1995; *Mura et al.*, 2002]. Additionally, a population of heavy neutral atoms (O, CO_2) are sputtered by accelerated heavy ions from the upper atmosphere [*Luhmann and Kozyra*, 1991], but their energies, though above the escape energy, are too low to be detected by conventional ENA detectors.

[4] The analyzer of space plasmas and energetic atoms (ASPERA-3) on the Mars Express spacecraft has observed ENAs originating from the upstream solar wind, the shocked solar wind in the magnetosheath, the picked-up planetary protons, and the scattered atoms by the upper atmosphere [*Gunell et al.*, 2006; *Futaana et al.*, 2006a, 2006b; *Brinkfeldt et al.*, 2006; *Galli et al.*, 2006, 2008]. These observations identified emissions from the subsolar region of the magnetosheath and from the flank region to the Martian tail. Some of these ENA emissions are highly anisotropic and form a jet or a cone that is tangential to the streamlines in the magnetosheath [*Futaana et al.*, 2006b]. However, the global morphology and, in particular, the factors that control the global distribution have not been established.

[5] The structure of this paper is as follows: In section 2, we first introduce the neutral particle detector (NPD) of the ASPERA-3 instrument package and its data set. Then, we apply a new processing method to extract and display the ENA direction distribution. In section 3, we describe the results, namely, the maps of the ENA emissions from the subsolar magnetosheath, the detection probability distribution, and the dependence of the ENA flux on several space environment proxies. In section 4, we interpret the results and discuss their implications. Section 5 concludes the paper.

2. Instrumentation and Data Processing

[6] The NPD consists of two identical sensors, NPD1 and NPD2, which are pinhole ENA cameras with a 10° (elevation) ×90° (azimuth) field of view divided into three viewing sectors [*Barabash and Lundin*, 2006]. The shape of the response function within each sector is Gaussian in both elevation and azimuth angles [*Grigoriev*, 2007]. The full width at half maximum of the Gaussian response function defines the angular resolution for each sector: 5° (elevation) ×∼40° (azimuth). The NPD is a time-of-flight velocity analyzer. The particles entering the instrument first pass the electrostatic deflector system, which removes the charged component and collimates the incoming beam. Then, the ENAs hit the start surface, a specially prepared ultrasmooth multilayer structure. This impact releases secondary electrons, which are guided toward and recorded by the start microchannel plates (MCP) to give a start pulse for the time-of-flight (TOF) system. The ENAs are reflected toward the stop surface (graphite covered by MgO), hit the surface, and again release secondary electrons, which are recorded by the stop MCPs, thus generating a stop pulse and giving the azimuthal direction. The time between the start and the stop pulses and the known TOF distance give the particle velocity. The TOF window is 50 ns–1900 ns, corresponding to the 10 eV–15 keV energy range for hydrogen. The two NPD sensors are accommodated with their field of view (FOV) planes ±15° from the plane perpendicular to the spacecraft velocity and the projection of six viewing directions on this plane covers ∼180° facing Mars (Figure 1 of *Futaana et al.* [2006b]). In this study, the instrument is considered a 5 pixel ENA telescope (the NPD 1 direction 0 was not used).

[7] To obtain the best possible statistics, we utilize the full set of "bin mode" data, which constitute the largest data set available for NPD [*Grigoriev*, 2007]. The data set covers the period from 14 March to 9 July 2004. The data in the bin mode are processed directly on board, and only valid events (start and stop within the allowed TOF window) are recorded and binned in the azimuth direction TOF matrix. Mars was exposed to a strong solar eruption on 07 June 2004, which strongly enhanced the ENA emissions [*Futaana et al.*, 2006c]. We specifically excluded this extreme event from the data set to prevent any potential bias in the global picture. In this study, the data are preprocessed to be the time series of data records with a 1 s interval. Each data record contains one TOF spectrum, i.e., the particle count rate as a function of TOF and the corresponding metadata (such as the

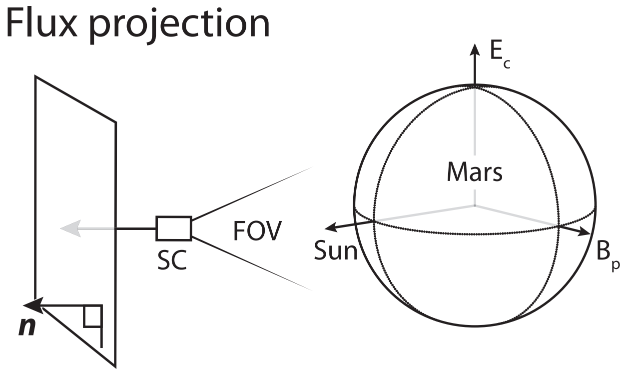

Figure 2. Geometry of the ENA flux calculations. For an arbitrary vector (**n**) in the MSE coordinate system, we select all NPD measurements along this direction independent of the spatial location of the sources and the spacecraft position. The fluxes are mapped on a plane perpendicular to (**n**). The map is a "geometric print" of the emitting region for a single direction. $\mathbf{E_c}$ and $\mathbf{B_p}$ represent the direction of the convective electric field and the magnetic field component perpendicular to the Sun-Mars line, respectively.

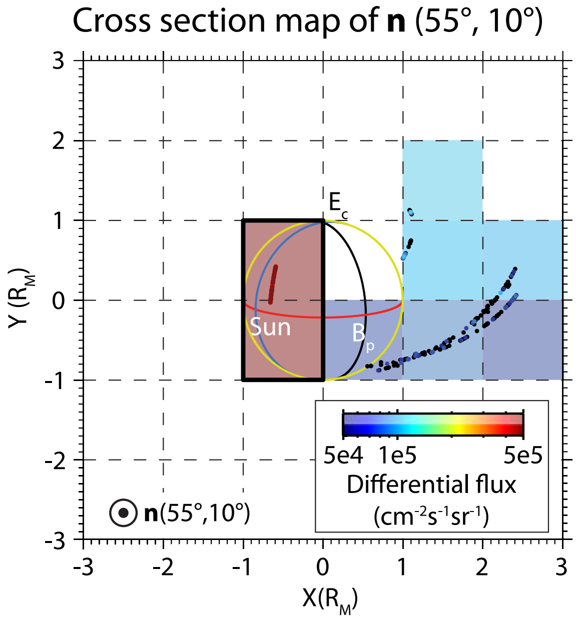
Cross section map of **n** (55°, 10°)

Figure 3. A “geometric map” of ENA fluxes for the direction **n** (azimuth 55°, elevation 10°) corresponding to Figure 2. The yellow circle represents the disk of Mars. The colored dots represent the observed fluxes and their corresponding positions. A square cell is assigned the maximal observed flux from all observations in this cell. The cells within the thick black line cover the subsolar region (see the text for definition). The red curve on the surface of Mars is in the plane of the magnetic field and the sunward direction; the black curve is the terminator; the blue curve is in the plane of the electric field and the sunward direction.

spacecraft position and attitude). We first clean up all data by removing nonphysical spikes and corrupted records. In addition, orbits with an insufficient number of records (≤ 7) are removed from the data set. After this step, a total number of 1.9×10^6 records (TOF spectra) are identified. Then, we remove the background signal due to UV photons by subtracting the count rate in the last TOF channel because the response of the sensor to UV radiation is uniform over all TOF channels [*Futaana et al.*, 2006c] (Figure 1). We select the TOF window from 100 ns to 309 ns and exclude both channels that are too fast and may be contaminated by internally produced electrons and channels that are too slow and may include oxygen ENAs. This TOF range corresponds to the energy range of 0.3–3 keV for hydrogen ENAs. The integral ENA flux is calculated by integrating the spectra over the selected TOF range.

[8] We use the Mars-centered solar electric field (MSE) for a frame of reference. The *X*, *Y*, and *Z* axes are defined by the directions of the Mars-Sun vector, the transverse-flow component ($\mathbf{B_p}$) of the interplanetary magnetic field (IMF), and the convective electric field ($\mathbf{E_c}$), respectively. The solar wind velocity is assumed to be in the *X* direction. Because Mars Express does not carry a magnetometer, we employ the concurrent IMF draping direction observed by the Mars Global Surveyor (MGS) as the IMF direction [*Brain et al.*, 2006]. This approach has been validated, for example, by comparing with ion-beam events that are correlated to Martian plasma sheet crossings [*Carlsson et al.*, 2008]. Obtaining a comprehensible ENA image of the Martian magnetosheath from Mars Express is a challenging problem. First, the ENA fluxes are neither directionally isotropic nor spatially homogeneous; for a single vantage point, only a very small fraction of the ENA fluxes can be recorded. Second, the observations from Mars Express are conducted at close proximity to the emitting region. Each orbit provides only limited coverage of the emitting region and the direction, which are not sufficient to obtain the full morphological picture of the ENA distribution. If the NPD is pointing to the direction of an ENA beam but the spacecraft is not in the beam, we call this situation “suboptimized observational geometry” herein. To cope with all of these problems, we develop a special projection method, which allows an ENA image of the whole interaction region to be built.

[9] We first convert the raw count rate for each NPD viewing sector to differential flux in $\mathrm{cm^{-2}s^{-1}sr^{-1}}$ using the

A: Differential flux distribution

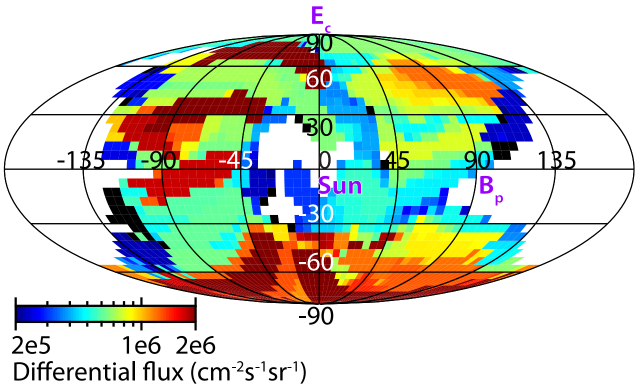

B: Accumulated weight distribution

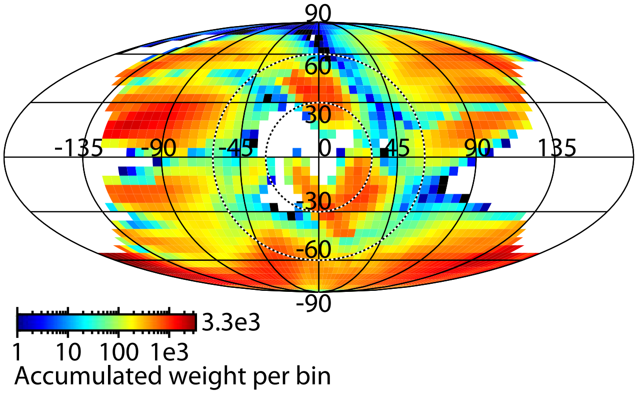

Figure 4. Direction dependence of (a) differential flux of ENAs emitted from the subsolar region of Mars and (b) accumulated weight w_{ij} (see text for the definition). The results are in the MSE coordinate system using Mollweide projections. In the white area, no data are available. The directions of the Sun, $\mathbf{B_p}$ and $\mathbf{E_c}$, are marked as defined in Figure 2a. The dashed circles in panel (b) show the 30° and 60° cone angles. Cone angle is the angle between the direction of the Sun and the direction of the spacecraft from a viewpoint on the surface of Mars.

Table 1. The Flux Ranges and the Total Accumulated Weights of the Four Groups

No.	Flux Range ($cm^{-2}s^{-1}sr^{-1}$)	$\sum_{i,j} w_{ij,g}$ ($\times$ 10^5)
1	$< 10^5$	3.26
2	$10^5 - 5 \times 10^5$	13.2
3	$5 \times 10^5 - 10^6$	2.08
4	$> 10^6$	0.256

calibrated conversion factor. Each NPD viewing direction is defined by the central bore-sight line for the respective sector. For an arbitrary vector (**n**) in the MSE coordinate system (Figure 2), we select the NPD measurements along this direction from the whole data set for all locations of the sources and the spacecraft. The fluxes are mapped onto a plane perpendicular to **n** and binned to a certain cell size to build up a map. The map is a "geometric print" of the emitting region for a single direction. Figure 3 shows an example of such a map.

[10] The cell size in the mapping plane should be larger than the actual scale subtending the instrumental FOV ($\sim 0.2 R_M$ for a typical spacecraft altitude of 1000 km) but smaller than the typical scale of the ENA source region, which is $\sim 2R_M$ [*Futaana et al.*, 2006c]. Therefore, in this study, we use $1R_M \times 1R_M$ to obtain as good coverage as possible. Each cell is assigned the maximum differential flux of the records it covers. We choose the maximum value instead of the mean or median value in a cell because a lower flux can be caused by suboptimized observational geometry, which results in smeared higher flux events. We then average the fluxes over selected cells for each map. In this study, we consider the emissions from the subsolar region only because (1) this region is the source of the highest ENA fluxes due to the highest neutral density and the lowest IMB altitude [*Kallio et al.*, 1997; *Futaana et al.*, 2006a, 2006b, 2011] and (2) the data set has full directional coverage (4π steradian) over this region. In the data processing, the subsolar region is defined as the region with a solar zenith angle $< 45°$ on the surface of Mars. From each geometric print map, we select only the cells covering the subsolar region (cells in the black box in Figure 3) in the analysis. This procedure has been repeated for all directions. The interval between directions, i.e., the angular resolution of the ENA direction map, is 5° in both the azimuth and the elevation.

3. Results

3.1. Global Mapping of ENA Emissions

[11] The distribution of the ENA fluxes for different emission directions is shown in Figure 4a in the Mollweide projection. Each pixel shows the average flux of the selected cells in the cross section map of this direction (e.g., the differential flux value in the direction (55°, 10°) is the average of the two red cells in Figure 3). Because the spacecraft was always outside the subsolar source region and because the spatial distribution of the source had been neglected, this map can be interpreted as an emission pattern of a point source.

[12] The angular resolution of the NPD sensor is ~40°, and the accuracy of the IMF clock angle, as determined by the accuracy of the IMF draping angle, is not more than 90° [*Brain et al.*, 2006]. Due to these uncertainties, we should not discuss finer features. With this consideration in mind, the map exhibits the following features: (1) The ENA emissions in the directions of 90° cone angle (the angle between the direction of the Sun and the direction of the spacecraft from a viewpoint on the surface of Mars) are generally stronger compared to those in the sunward direction. All of the measurements with a flux higher than 10^6 $cm^{-2}s^{-1}sr^{-1}$ are observed close to 90° cone angle directions. 2) Within the plane of the 90° cone angle, ENA fluxes are enhanced in the $-\mathbf{E_c}$ direction.

[13] Different production mechanisms result in ENA emissions of different strengths and angular distributions. We therefore investigate how the measurements are distributed as a function of the flux to separate these various production mechanisms. We divide the whole data set into four groups according to the ENA differential flux value (Table 1). For the whole data set, we calculate the accumulated weight distribution, w_{ij}, for each pixel (direction

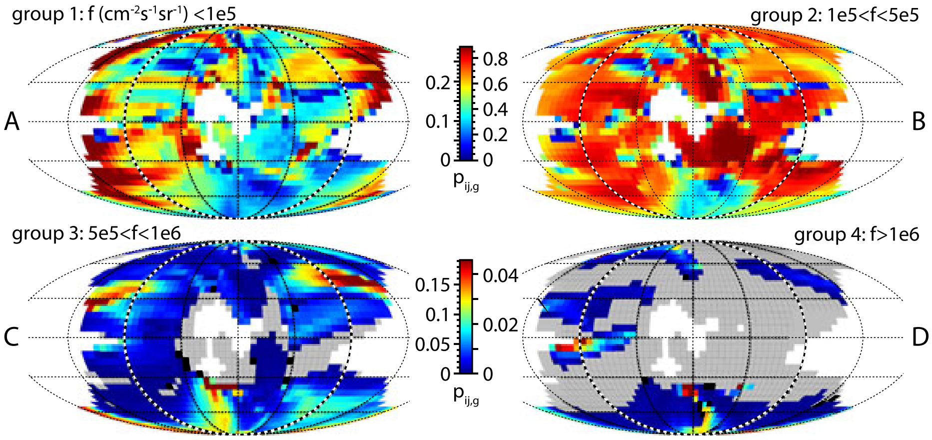

Figure 5. Detection probability distribution ($p_{ij,g}$). Each map describes one group in the flux range shown in the corner in units of $cm^{-2}s^{-1}sr^{-1}$. See the text for the definition of $p_{ij,g}$. There are no measurements for the white area. In the gray area, $p_{ij,g}$ = 0. The dashed curve on top shows the 90° cone angle.

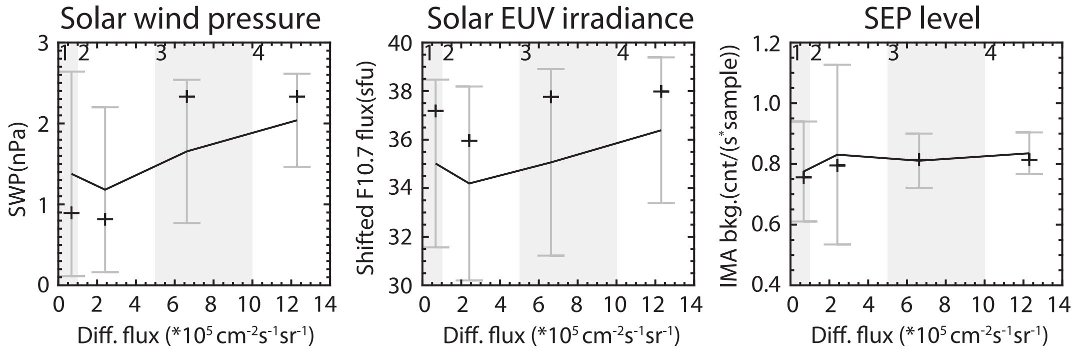
Solar wind pressure

Solar EUV irradiance

SEP level

Figure 6. Dependencies of the ENA fluxes on the space environmental conditions. From left to right: solar wind dynamical pressure (P_{dyn}), solar F10.7 radiation flux shifted to Mars and SEP level represented by the background count rate of ASPERA-3/Ion Mass Analyzer (IMA). In each panel, the shadowed and blank rectangles in the background indicate the flux ranges of the four groups numbered in the top left corner; the black curve, the black pluses, and the gray error bars show the mean values, the median values and the ±1 standard deviation from the mean values of the proxy in the four groups, respectively.

$\mathbf{n}_{ij}$, for the ith azimuth bin and the jth elevation bin). w_{ij} is defined as follows:

$$w_{ij} = \sum_{m}^{\text{all observations}} p_m(\mathbf{n}_{ij}) \tag{1}$$

where p_m is the instrument response function ($0 \leq p_m(\mathbf{n}_{ij}) \leq 1$) in the direction $\mathbf{n}_{ij}$. $p_m = 1$ when $\mathbf{n}_{ij}$ aligns with the bore-sight direction. The response function is Gaussian over the FOV and is centered at the bore-sight direction (section 2). Figure 4b shows the distribution of w_{ij}. A direction $\mathbf{n}_{ij}$ with a larger w_{ij} means that we have more observations in the direction $\mathbf{n}_{ij}$. Similarly, $w_{ij,g}$ can be defined for each flux group g.

[14] We now define the detection probability distribution $p_{ij,g} = w_{ij,g}/w_{ij}$. A higher $p_{ij,g}$ indicates a higher probability of observing the flux within the flux group g in $\mathbf{n}_{ij}$. The $p_{ij,g}$ distributions for the four groups are shown in Figure 5.

[15] ENA fluxes of low intensity (group 1 and 2) are emitted in almost all directions. The emission patterns are almost isotropic, with a slightly higher probability for emissions in the antisunward directions (toward the night side, cone angle >90°). Group 2 also includes emissions toward the Sun (cone angle <50°). An ENA flux of high intensity (group 3) has never been observed in the sunward direction (cone angle <30°). Strong emissions thus tend to occur nearly perpendicular to the solar wind flow. In group 4, the highest flux group, all emissions occur in the perpendicular direction, with an angular width of ~30°. Moreover, these results indicate a preference for the $-E_c$ direction. The features of the detection probability distributions in groups 3 and 4 explain the directional distribution of the ENA flux (Figure 4a): higher ENA fluxes in the direction perpendicular to the solar wind flow.

3.2. Correlation With the Upstream Conditions

[16] We also investigate the dependences of the ENA emissions in different flux ranges on the parameters characterizing the space environment, namely, the solar wind dynamic pressure P_{dyn}, the solar EUV irradiance and the solar energetic particle (SEP) flux (Figure 6). For P_{dyn}, we use the proxy based on the MGS magnetometer (MAG) measurements inside the Martian induced magnetosphere by assuming that the solar wind pressure is balanced by the magnetic pressure [*Crider et al.*, 2003]. For solar EUV irradiance, we use the F10.7 flux measurement on Earth shifted to Mars, as in *Mitchell et al.* [2001]. For the SEP level, we take the background count rate of ASPERA-3/IMA as an indicator. The correlation between the IMA background count rate and the SEP flux was demonstrated by *Futaana et al.* [2008]. We can identify positive correlations to the solar wind dynamic pressure. The higher mean value of P_{dyn} in the lowest flux group may be caused by sub-optimized observation geometries in which only low ENA fluxes are observed. No significant dependences on the solar EUV irradiance or the SEP level could be confirmed despite large variations in the ENA fluxes of each group.

4. Discussion

4.1. Dependence on the Solar and Solar Wind Conditions

[17] The ENA fluxes are given by the line-of-sight integrals

$$J_{\mathrm{ENA}}(\mathbf{r}, E, \mathbf{u}) = \sigma(E) \int_0^\infty \mathrm{d}s\, N(\mathbf{r} - \mathbf{u}s) \cdot J_{\mathrm{ion}}(\mathbf{r} - \mathbf{u}s, E, \mathbf{u}) \tag{2}$$

where $\sigma(E)$ is the energy-dependent cross section, $\mathbf{r}$ is the position of the vantage point, $\mathbf{u}$ is the direction of the velocity vector of the ENAs, $N(\mathbf{r} - \mathbf{u}s)$ and $J_{\mathrm{ion}}(\mathbf{r} - \mathbf{u}s, E, \mathbf{u})$ is the neutral density and the ion differential flux at the point of ENA generation. The integration is performed along the line-of-sight s.

[18] The increase in the ion flux results in a respective increase in the ENA flux. The dependence of the ENA flux on the dynamic pressure, which is proportional to the product of the ion flux and velocity, should be even stronger. The induced magnetosphere boundary moves closer to Mars as the dynamic pressure increases. The magnetosheath ions thus reach lower altitudes with a higher neutral density. Because the neutral density increases exponentially with the decrease of height, the ENA flux increases strongly. Indeed, an increase in the dynamic pressure by a factor of two results in an increase in the ENA fluxes by a factor of 6 (Figure 6).

[19] The ENA flux and the solar EUV irradiance have a complex relationship. The exospheric scale height increases

(due to the temperature increase) with the EUV flux, but the neutral density at the fixed location may decrease due to enhanced escape [e.g., *Krasnopolsky*, 2010]. Using the current data set, we could not identify a strong correlation, although a small positive correlation is evident (Figure 6).

[20] The weak correlation between the ENA flux and the SEP level is not surprising given the limited influence of SEPs on the exobase temperature [*Leblanc and Johnson*, 2002].

4.2. Morphology of the ENA Emissions in Different Flux Groups

[21] The different distributions of ENA emissions reflect different origins of the detected ENAs. Due to the crude energy resolution of the instrument mode used in this analysis ($\Delta E/E \sim 50\%$), comparing the energy spectra of the ENAs among different flux groups is difficult. Thus, we rely on the purely morphological features of the obtained images for our interpretation in this study.

[22] The isotropic distribution of the low flux emissions and the slight preference for the sunward directions shown in group 2 suggest that these low flux ENAs result from backscattering of the ENAs created upstream of the bow shock and in the magnetosheath, instead of being neutralized in the magnetosphere. Indeed, recent studies of the solar wind proton entry and transport in the Martian induced magnetosphere revealed that plasma entry below the induced magnetosphere boundary is rare and sporadic [*Diéval et al.*, 2012; *Shematovich et al.*, 2011]. Moreover, the protons that penetrate the induced magnetosphere boundary hardly reach the exobase because these protons are deflected by the magnetic field of the induced magnetosphere in the magnetic barrier (or pile up) region [*Vignes et al.*, 2000]. The only component that may reach the exobase and collide with the upper atmosphere is the ENAs produced above the IMB.

[23] *Kallio et al.* [1997] showed that 1%–3% of the solar wind particles are converted to neutral particles in the extended Martian exosphere via charge exchange outside the bow shock. Approximately 15–20% of the hydrogen atoms reaching the exobase are then backscattered [*Shematovich et al.*, 2011]. Therefore, the expected differential flux of the backscattered ENAs produced upstream of the bow shock in $\mathrm{cm^{-2}s^{-1}sr^{-1}}$ would be $0.03 \times 0.2 F_{\mathrm{sw}}/2\pi = 10^{-3} F_{\mathrm{sw}}$, where F_{sw} is the solar wind flux in $\mathrm{cm^{-2}s^{-1}}$. For the typical $F_{\mathrm{sw}} = 10^8$ $\mathrm{cm^{-2}s^{-1}}$, we obtain a differential flux of the backscattered ENAs of approximately 10^5 $\mathrm{cm^{-2}s^{-1}sr^{-1}}$, which is indeed close to the observed flux $3 \times 10^5 \mathrm{cm^{-2}s^{-1}sr^{-1}}$. The ENAs produced in the magnetosheath will also precipitate onto the exobase. The backscattered ENA flux should thus be even higher and better match our observations.

[24] The high-flux ENA emissions (groups 3 and 4) in the perpendicular direction to the solar wind and asymmetrical with respect to the convective electric field are the result of charge exchange between the magnetosheath plasma with the exospheric neutrals. In an earlier study, the authors reported 4–7×10^5 $\mathrm{cm^{-2}s^{-1}sr^{-1}}$ for the same (0.3–3 keV) energy range [*Futaana et al.*, 2006b] for this population. These ENAs reflect the pattern of the proton flux distribution above the induced magnetosphere boundary. We discuss this issue separately in section 4.3.

[25] The charge exchange of the magnetosheath plasma has been modeled in detail (for example, [*Kallio et al.*, 1997; *Holmström et al.*, 2002]) using the empirical model of the plasma flow distribution in the magnetosheath [*Kallio*, 1996]. The assumed cylindrical symmetry in the plasma flowing around the induced magnetosphere results in cylindrically symmetrical ENA emissions because ENAs are emitted tangential to the plasma stream lines over relatively short distances, where the stream line is closest to the planet (highest neutral density). *Holmström et al.* [2002] calculated the ENA flux (in $\mathrm{cm^{-2}s^{-1}}$) through the $3 \times R_m$ sphere as a function of the cone angle and showed that the maximum flux occurred around 110° cone angle, i.e., close to the results from our observations.

[26] The morphology of the ENA emissions from Mars can be described as follows. The Martian dayside emits a relatively weak isotropic ENA flux ($\sim 10^5 \mathrm{cm^{-2}s^{-1}sr^{-1}}$) resulting from the backscattering of the neutralized solar wind at the exobase. In an analogy to optics, this component may be referred to as ENA "glow". The charge exchange of the magnetosheath protons results in ENA emissions with a maximum flux flowing in a nearly perpendicular plane to the solar wind (cone angle ~90°). At great distances from Mars, these emissions resemble a thick layer or even a wall. Within the ENA wall, these emissions increase slightly along the $-\mathbf{E_c}$ direction. In previous studies based on single orbits [*Futaana et al.*, 2006b; *Grigoriev et al.*, 2006], crossing the ENA wall resulted in a sharp increase in the ENA flux, which was called an ENA "jet". The statistical study presented here reveals a more homogeneous distribution and most likely only a weak "jet" close to the $-\mathbf{E_c}$ direction.

4.3. Asymmetry With Respect to the Convective Electric Field

[27] The observed increase (a factor of 2–3) in the ENA flux in the $-\mathbf{E_c}$ direction reflects the kinetic instead of hydrodynamic nature of the solar wind Mars interaction. The asymmetry cannot be related to the charge exchange of the planetary protons because the latter increases in the $+\mathbf{E_c}$ direction [*Lichtenegger et al.*, 2002].

[28] An asymmetric shape of the IMB is the reason that may cause a higher ENA flux in the $-\mathbf{E_c}$ direction. MGS observed that the magnetic pressure in the magnetic pileup region is lower in the hemisphere, where $\mathbf{E_c}$ is locally downward ($-\mathbf{E_c}$ hemisphere) [*Vennerstrom et al.*, 2003]. A lower IMB is thus found in the $-\mathbf{E_c}$ hemisphere. The combined magnetic field and plasma observations reveal the same trend for the IMB position at mid-to-high solar zenith angles [*Dubinin et al.*, 2006; *Edberg et al.*, 2009]. However, numerical simulations cannot explain this feature. Hybrid models studying the $\pm\mathbf{E_c}$ asymmetry [*Brain et al.*, 2010] show that the IMB and bow shock positions are generally higher in the $-\mathbf{E_c}$ hemisphere.

[29] Our observation of higher ENA flux in the $-\mathbf{E_c}$ direction agrees with the asymmetry of the IMB position obtained statistically from in situ observations. A lower IMB position in the $-\mathbf{E_c}$ hemisphere allows magnetosheath protons to reach the lower and thus denser exosphere, producing a more intense ENA flux via the charge exchange reaction. Explaining how a higher IMB position, as in the models, may increase the ENA flux is difficult. The discrepancy between the models and observations, both in situ and remote, is beyond the scope of this paper and should be addressed in modeling papers. This asymmetry is more evident

during enhanced ENA emissions when the solar wind dynamic pressure is high.

5. Conclusion

[30] A statistical analysis of the ENA measurements during the period from 14 March to 9 July 2004 reveals the general morphology of the ENA emissions from Mars. The dayside of the planet is a source of weak isotropic emissions resulting from the backscattering of the neutralized solar wind. The neutralized solar wind is generated by the charge exchange of the solar wind protons on the Martian exosphere, which extends well beyond the bow shock. The shocked solar wind protons in the magnetosheath region form emissions peaked in the directions of the 90° cone angle. The emission pattern is, in general, uniform over the clock angles and resembles a wall or layer with an increase in the intensity in the $-\mathbf{E_c}$ direction. No pronounced jets are identified, although the emissions may appear as a jet to an observer crossing the ENA wall. This $\pm\mathbf{E_c}$ asymmetry, the higher ENA flux in the $-\mathbf{E_c}$ direction by a factor of 2–3, is consistent with the asymmetric shape of the IMB revealed by previous observations. However, this result has not been reproduced in numerical simulations. In addition, we demonstrate the positive correlation between the ENA flux and the solar wind dynamic pressure. This correlation can be explained by the compression of the induced magnetosphere during a high dynamic pressure event, which allows the shocked solar wind to reach the lower and therefore denser exosphere.

[31] **Acknowledgments.** This work by X.-D. Wang is supported by the Swedish National Space Board via a dedicated grant. The authors would like to thank D. Brain, D. Mitchell, and D. Crider for providing the MGS IMF draping direction, the solar wind dynamic pressure, and the solar EUV irradiance proxies at Mars.

[32] Masaki Fujimoto thanks Philippe Garnier and Andrei Fedorov for their assistance in evaluating this paper.

References

Barabash, S., R. Lundin, T. Zarnowiecki, and S. Grzedzielski (1995), Diagnostic of energetic neutral particles at Mars by the ASPERA-C instrument for the Mars 96 mission, *Adv. Space Res.*, *16*(4), 81–86, doi:10.1016/0273-1177(95)00212-W.

Barabash, S., and R. Lundin (2006), ASPERA-3 on Mars Express, *Icarus*, *182*(2), 301–307, doi:10.1016/j.icarus.2006.02.015.

Barabash, S., et al. (2006), The Analyzer of Space Plasmas and Energetic Atoms (ASPERA-3) for the Mars Express mission, *Space Sci. Rev.*, *126*(1-4), 113–164, doi:10.1007/s11214-006-9124-8.

Barabash, S., et al. (2007), The Analyser of Space Plasmas and Energetic Atoms (ASPERA-4) for the Venus Express mission, *Planet. Space Sci.*, *55*(12), 1772–1792, doi:10.1016/j.pss.2007.01.014.

Barabash, S., et al. (2009), Investigation of the solar wind-Moon interaction onboard Chandrayaan-1 mission with the SARA experiment, *Curr. Sci.*, *96*(4), 526–532.

Brain, D., et al. (2010), A comparison of global models for the solar wind interaction with Mars, *Icarus*, *206*(1), 139–151, doi:10.1016/j.icarus.2009.06.030.

Brain, D. A., D. L. Mitchell, and J. S. Halekas (2006), The magnetic field draping direction at Mars from April 1999 through August 2004, *Icarus*, *182*(2), 464–473, doi:10.1016/j.icarus.2005.09.023.

Brinkfeldt, K., et al. (2006), First ENA observations at Mars: Solar-wind ENAs on the nightside, *Icarus*, *182*(2), 439–447, doi:10.1016/j.icarus.2005.12.023.

Carlsson, E., D. Brain, J. Luhmann, S. Barabash, A. Grigoriev, H. Nilsson, and R. Lundin (2008), Influence of IMF draping direction and crustal magnetic field location on Martian ion beams, *Planet. Space Sci.*, *56*(6), 861–867, doi:10.1016/j.pss.2007.12.016.

Crider, D. H., D. Vignes, A. M. Krymskii, T. K. Breus, N. F. Ness, D. L. Mitchell, J. A. Slavin, and M. H. Acuña (2003), A proxy for determining solar wind dynamic pressure at Mars using Mars Global Surveyor data, *J. Geophys. Res.*, *108*(A12), 1461, doi:10.1029/2003JA009875.

Diéval, C., et al. (2012), A case study of proton precipitation at Mars: Mars Express observations and hybrid simulations, *J. Geophys. Res.*, *117*, A06222, doi:10.1029/2012JA017537.

Dubinin, E., M. Fränz, J. Woch, E. Roussos, S. Barabash, R. Lundin, J. Winningham, R. Frahm, and M. Acuña (2006), Plasma morphology at Mars. Aspera-3 observations, *Space Sci. Rev.*, *126*, 209–238, doi:10.1007/s11214-006-9039-4.

Edberg, N. J. T., D. A. Brain, M. Lester, S. W. H. Cowley, R. Modolo, M. Fränz, and S. Barabash (2009), Plasma boundary variability at Mars as observed by Mars Global Surveyor and Mars Express, *Ann. Geophys.*, *27*, 3537–3550, doi:10.5194/angeo-27-3537-2009.

Futaana, Y., et al. (2006a), First ENA observations at Mars: ENA emissions from the Martian upper atmosphere, *Icarus*, *182*(2), 424–430, doi:10.1016/j.icarus.2005.09.019.

Futaana, Y., et al. (2006b), First ENA observations at Mars: Subsolar ENA jet, *Icarus*, *182*(2), 413–423, doi:10.1016/j.icarus.2005.08.024.

Futaana, Y., S. Barabash, A. Grigoriev, D. Winningham, R. Frahm, M. Yamauchi, and R. Lundin (2006c), Global response of Martian plasma environment to an interplanetary structure: From ENA and plasma observations at Mars, *Space Sci. Rev.*, *126*, 315–332, doi:10.1007/s11214-006-9026-9.

Futaana, Y., et al. (2008), Mars Express and Venus Express multi-point observations of geoeffective solar flare events in December 2006, *Planet. Space Sci.*, *56*(6), 873–880, doi:10.1016/j.pss.2007.10.014.

Futaana, Y., J.-Y. Chaufray, H. Smith, P. Garnier, H. Lichtenegger, M. Delva, H. Gröller, and A. Mura (2011), Exospheres and energetic neutral atoms of Mars, Venus and Titan, *Space Sci. Rev.*, *162*(1), 213–266, doi:10.1007/s11214-011-9834-4.

Galli, A., P. Wurz, S. Barabash, A. Grigoriev, H. Gunell, R. Lundin, M. Holmström, and A. Fedorov (2006), Energetic hydrogen and oxygen atoms observed on the nightside of Mars, *Space Sci. Rev.*, *126*, 267–297, doi:10.1007/s11214-006-9088-8.

Galli, A., P. Wurz, E. Kallio, A. Ekenbäck, M. Holmström, S. Barabash, A. Grigoriev, Y. Futaana, M.-C. Fok, and H. Gunell (2008), Tailward flow of energetic neutral atoms observed at Mars, *J. Geophys. Res.*, *113*, E12012, doi:10.1029/2008JE003139.

Grigoriev, A. (2007), The neutral particle detector on the Mars and Venus Express missions, PhD thesis, Swed. Inst. of Space Phys., Kiruna, Swed.

Grigoriev, A., Y. Futaana, S. Barabash, and A. Fedorov (2006), Observations of the Martian subsolar ENA jet oscillations, *Space Sci. Rev.*, *126*(1), 299–313, doi:10.1007/s11214-006-9121-y.

Gunell, H., et al. (2006), First ENA observations at Mars: Charge exchange ENAs produced in the magnetosheath, *Icarus*, *182*(2), 431–438, doi:10.1016/j.icarus.2005.10.027.

Holmström, M., S. Barabash, and E. Kallio (2002), Energetic neutral atoms at Mars 1. Imaging of solar wind protons, *J. Geophys. Res.*, *107*(A10), 1277, doi:10.1029/2001JA000325.

Kallio, E. (1996), An empirical model of the solar wind flow around Mars, *J. Geophys. Res.*, *101*(A5), 11,133–11,147, doi:10.1029/96JA00164.

Kallio, E., and S. Barabash (2001), Atmospheric effects of precipitating energetic hydrogen atoms on the Martian atmosphere, *J. Geophys. Res.*, *106*(A1), 165–177, doi:10.1029/2000JA002003.

Kallio, E., and P. Janhunen (2001), Atmospheric effects of proton precipitation in the Martian atmosphere and its connection to the Mars-solar wind interaction, *J. Geophys. Res.*, *106*(A4), 5617–5634, doi:10.1029/2000JA000239.

Kallio, E., J. G. Luhmann, and S. Barabash (1997), Charge exchange near Mars: The solar wind absorption and energetic neutral atom production, *J. Geophys. Res.*, *102*(A10), 22,183–22,197, doi:10.1029/97JA01662.

Krasnopolsky, V. A. (2010), Solar activity variations of thermospheric temperatures on Mars and a problem of CO in the lower atmosphere, *Icarus*, *207*(2), 638–647, doi:10.1016/j.icarus.2009.12.036.

Krimigis, S., et al. (2004), Magnetosphere Imaging Instrument (MIMI) on the Cassini mission to Saturn/Titan, *Space Sci. Rev.*, *114*(1-4), 233–329, doi:10.1007/s11214-004-1410-8.

Leblanc, F., and R. E. Johnson (2002), Role of molecular species in pickup ion sputtering of the Martian atmosphere, *J. Geophys. Res.*, *107*(E2), 5010, doi:10.1029/2000JE001473.

Lichtenegger, H., H. Lammer, and W. Stumptner (2002), Energetic neutral atoms at Mars 3. Flux and energy distributions of planetary energetic H atoms, *J. Geophys. Res.*, *107*(A10), 1279, doi:10.1029/2001JA000322.

Luhmann, J. G., and J. U. Kozyra (1991), Dayside pickup oxygen ion precipitation at Venus and Mars: Spatial distributions, energy deposition and consequences, *J. Geophys. Res.*, *96*(A4), 5457–5467, doi:10.1029/90JA01753.

McComas, D., et al. (2009), IBEX—Interstellar boundary explorer, *Space Sci. Rev.*, *146*(1-4), 11–33, doi:10.1007/s11214-009-9499-4.

Mitchell, D., et al. (2000), High energy neutral atom (HENA) imager for the IMAGE mission, *Space Sci. Rev.*, *91*(1-2), 67–112, doi:10.1023/A:1005207308094.

Mitchell, D. L., R. P. Lin, C. Mazelle, H. Réme, P. A. Cloutier, J. E. P. Connerney, M. H. Acuña, and N. F. Ness (2001), Probing Mars' crustal magnetic field and ionosphere with the MGS electron reflectometer, *J. Geophys. Res.*, *106*(E10), 23,419–23,427, doi:10.1029/2000JE001435.

Moore, T., et al. (2000), The low-energy neutral atom imager for IMAGE, *Space Sci. Rev.*, *91*(1-2), 155–195, doi:10.1023/A:1005211509003.

Mura, A., A. Milillo, S. Orsini, E. Kallio, and S. Barabash (2002), Energetic neutral atoms at Mars 2. Imaging of the solar wind-Phobos interaction, *J. Geophys. Res.*, *107*(A10), 1278, doi:10.1029/2001JA000328.

Pollock, C., et al. (2000), Medium energy neutral atom (MENA) imager for the IMAGE mission, *Space Sci. Rev.*, *91*(1-2), 113–154, doi:10.1023/A:1005259324933.

Shematovich, V. I., D. V. Bisikalo, C. Diéval, S. Barabash, G. Stenberg, H. Nilsson, Y. Futaana, M. Holmstrom, and J.-C. Gèrard (2011), Proton and hydrogen atom transport in the Martian upper atmosphere with an induced magnetic field, *J. Geophys. Res.*, *116*, A11320, doi:10.1029/2011JA017007.

Vennerstrom, S., N. Olsen, M. Purucker, M. H. Acuña, and J. C. Cain (2003), The magnetic field in the pile-up region at Mars, and its variation with the solar wind, *Geophys. Res. Lett.*, *30*(7), 1369, doi:10.1029/2003GL016883.

Vignes, D., C. Mazelle, H. Réme, M. H. Acuña, J. E. P. Connerney, R. P. Lin, D. L. Mitchell, P. Cloutier, D. H. Crider, and N. F. Ness (2000), The solar wind interaction with Mars: Locations and shapes of the bow shock and the magnetic pile-up boundary from the observations of the MAG/ER Experiment onboard Mars Global Surveyor, *Geophys. Res. Lett.*, *27*(1), 49–52, doi:10.1029/1999GL010703.